

1 **Statistical characteristics of raindrop size**
2 **distribution during rainy seasons in Complicated**
3 **Mountain Terrain**

4 Wenqian Mao^{1,3,4}, Wenyu Zhang^{2,3,4}, Menggang Kou²

- 5 1. College of Resources and Environmental Sciences, Gansu Agricultural University, Lanzhou
6 730070, China
7 2. School of Geoscience and Technology, Zhengzhou University, Zhengzhou, 450001, China
8 3. Key Laboratory for Cloud Physics, Chinese Academy of Meteorological Sciences, Beijing
9 100081, China
10 4. College of Atmospheric Sciences, Lanzhou University, Lanzhou, 730000, China

11 Correspondence to: Wenqian Mao (mdycmwq@163.com)

12 **Abstract:** In order to improve understanding of the characteristics of raindrop size
13 distribution (DSD) over complex mountainous terrain, the differences in DSD over the
14 southern slopes, northern slopes and interior of the Qilian Mountains were analyzed
15 using six months of observations. For all rainfall events, the number concentrations of
16 small and large raindrops in the interior and on the southern slopes were greater than
17 on the northern slopes, but midsize raindrops were less. The DSD spectrum of the
18 interior was more variable and differed significantly from that of the northern slopes.
19 The differences in the normalized intercept parameters of the DSD for stratiform and
20 convective rainfall were 8.3% and 10.4%, respectively, and those of the **mass-weighted**
21 **mean diameters** were 10.0% and 23.4%, respectively, while the standard deviations of
22 DSD parameters at interior sites were larger. The differences in the coefficient and
23 exponent of the Z-R relationship were 2.5% and 10.7%, respectively, with an increasing
24 value of the coefficient from the southern to the northern slopes for stratiform rainfall,
25 but the opposite for convective rainfall. In addition, the DSD characteristics and Z-R
26 relationships were more similar at the ipsilateral sites and had smaller differences
27 between the southern slopes and interior of the mountains.

28
29 **Keywords:** *raindrop size distribution; complicated mountain terrain; spatial variation*
30

31 1 Introduction

32 Raindrop size distribution (DSD), the number of raindrops per drop size per unit
33 volume, is an important parameter to statistically describe the microstructure of
34 precipitation (Bringi et al., 2003; Ma et al., 2019a). The measurement of DSD can
35 provide some fundamental information such as raindrop size (D), liquid water content
36 (W), rain rate (R), radar reflectivity factor (Z) and so on, which has an essential
37 contribution to improving quantitative precipitation estimation (QPE) using weather
38 radar and satellite observations (Adirosi et al., 2018; Jash et al., 2019). The
39 parameterization of DSD can obtain the distribution model parameters of DSD in
40 different rain types, which is significant in advancing microphysics parameterization in
41 numerical weather prediction (NWP) models (Wainwright et al., 2014; McFarquhar et
42 al., 2015; Zhao et al., 2019). In addition, understanding the DSD is crucial in many
43 applied fields concerning hydrology, agriculture, soil erosion and microwave
44 communication (Rincon et al., 2002; Smith et al., 2009; Angulo-Martínez et al., 2015;
45 Lim et al., 2015; Yang et al., 2016).

46 Numerous studies have been carried out on the statistical characteristics of DSD
47 in different regions (Campos et al., 2006; Seela et al., 2017; Dolan et al., 2018; Protat
48 et al., 2019; Loh et al., 2019; Jash et al., 2019). It has been shown that the number
49 concentration and size of raindrops increase with rain rate and so the DSD becomes
50 higher and wider. The characteristics in different rain types demonstrate that the mass-
51 weighted mean diameter (i.e., D_m) and normalized intercept parameter (i.e., N_w) of
52 convective rainfall are larger than those of stratiform rainfall. Furthermore, these
53 studies also reveal that there are more differences in the characteristics of DSD. Dolan
54 et al. (2018) divided global DSD characteristics into 6 types by using 12 datasets across
55 three latitudes and found that the centralized regions and DSD parameters of the 6 types
56 varied in location. The average number of raindrops in central Korea was usually
57 greater than that in the southeast under three rainfall systems, especially drops in the
58 0.31–0.81mm diameter range (Loh et al., 2019). According to DSD measurements in
59 the Tibetan Plateau region, eastern areas have a higher raindrop number concentration
60 in the diameter range of 0.437–1.625 mm and greater variation in diameters than in
61 central areas (Wang et al., 2020). Compared to eastern China and northern China, the
62 DSD in southern China shows a higher number concentration of relatively small-sized
63 drops (Zhang et al., 2019). Comparison of the Z - R relationship (defined as $Z=AR^b$)
64 indicates that the coefficient decreases with increasing R in the southern Tibetan Plateau,
65 which is opposite to the case in southern China (Wu et al., 2017). For the DSD
66 parameters of stratiform and convective rainfall, there are various changes between the
67 lower and middle reaches of the Yangtze River (Fu et al., 2020).

68 As reported in the above studies, DSD characteristics vary significantly with
69 factors such as geographical location, climatic region and rain types. Pu et al. (2020)
70 analyzed the DSD characteristics of five sites in Nanjing city and found the N_w of DSD
71 to be largest at site near industrial areas, but the D_m of DSD was largest at sites near the
72 city's center. In other words, even at the smaller scale, there are still differences in the
73 microphysical characteristics reflected by the DSD, which is due to the influence of the
74 surrounding environment. How, then, do the characteristics of DSD vary from location

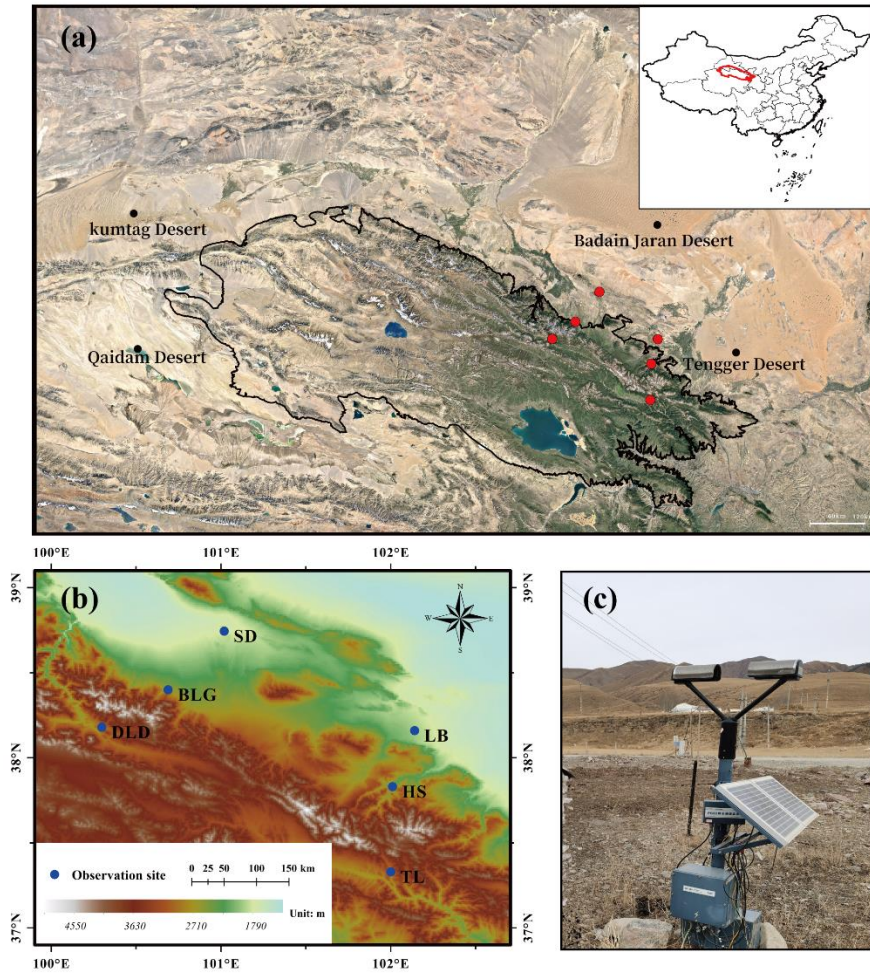
75 to location over the complicated mountain terrain? Rao et al. (2006), by comparing the
76 DSD parameters at different altitudes, suggested that the obvious variation in DSD with
77 altitude is related to the processes of evaporation and breakup. Using aircraft
78 observations, Geoffroy et al. (2014) concluded that the total concentration of raindrops
79 decreased while the average drop size increased with decreasing altitude. Han et al.
80 (2023) found the rain rate between $1 \leq R < 5 \text{ mm h}^{-1}$ to the total precipitation increases
81 with altitude by using the disdrometers data from 2434 m to 4202 m located in the
82 northeastern Tibetan Plateau. With more attention on mountain research, the concerning
83 question are growing. Such as how large might the differences in DSD be at different
84 altitudes in mountainous regions; and how significant might the effects be of these
85 differences?

86 The Qilian Mountains, a series of marginal mountains in the northeastern part of
87 the Tibetan Plateau, are a vitally important ecological protection barrier in the northwest
88 arid areas of the region, that block the connection between deserts and wilderness
89 (Figure 1a). The mountains form several inland rivers that are important water sources
90 for the arid areas of the northwest and have therefore made a considerable contribution
91 to regional economic development (Gou et al., 2005; Tian et al., 2014; Qin et al., 2016).
92 In this study, we chose the Qilian Mountains as the research object and selected six sites
93 with different backgrounds representing the southern slopes, northern slopes and
94 interior of the mountains. To thoroughly investigate the discrepancies in this complex
95 mountain terrain, the DSD characteristics and *Z-R* relationships were comprehensively
96 analyzed according to different rain types based on continuous disdrometer
97 observations in the rainy season. The primary goal was to obtain a deeper understanding
98 and characteristic differences of DSD over the Qilian Mountains and refine the accuracy
99 of QPE comparing with standard *Z-R* relationships in models, which could then be used
100 as a research foundation for developing cloud water resources in mountainous areas.

101 **2 Data and method**

102 **2.1 Sites and instruments**

103 The eastern and middle sections of the Qilian Mountains were chosen as the main
104 study area, taking into account that several important inland rivers originate from these
105 areas (Li et al., 2019). Six disdrometers were deployed on the southern slopes, northern
106 slopes and interior (close to the ridge) of the Qilian Mountains, with three sites in the
107 eastern section [called Taola (TL, 2910 m), Huangchengshuiguan (HS, 2342 m) and
108 Liuba (LB, 1926 m), from south to north] and another three sites in the middle section
109 [called Daladong (DLD, 2957 m), Boligou (BLG, 2455 m) and Shandan (SD, 1765 m),
110 from south to north]. The background of the Qilian Mountains is shown on the satellite
111 map in Figure 1a, and the six sites are marked on the topographical map, also in Figure
112 1b. The distances between the six sites are listed in Table 1. The sites in the south, north
113 and interior are basically parallel to the orientation of the mountains, and the sections
114 formed by the sites in the east and interior are basically perpendicular to it. On the basis
115 of an historical weather review and rain gauge observations, the rainy season at the six
116 sites is concentrated in May to October, with more precipitation in July, August and
117 September.



119
 120 Figure 1. (a) Geographical overview of the Qian Mountains; (b) the disdrometer sites
 121 (circles); (c) the observation device at TL site. Source: Google Earth © Google Earth
 122 YEAR

123 Table 1. Site details (latitude, longitude, sea level height) and distances (km) between
 124 pairs of sites.

Six sites	LB	HS	TL	SD	BLG	DLD
LB (38.16°N, 102.14°E, 1926m)	-	39.6	94.3	116.0	129.6	161.1
HS (37.83°N, 102.01°E, 2342m)	-	-	55.6	135.1	132.8	154.9
TL (37.33°N, 102.00°E, 2910m)	-	-	-	182.4	167.3	177.0
SD (38.80°N, 101.08°E, 1765m)	-	-	-	-	54.2	96.8
BLG (38.4°N, 100.69°E, 2455m)	-	-	-	-	-	43.3
DLD (38.18°N, 100.3°E, 2957m)	-	-	-	-	-	-

125 This study used an optical, laser-based device to measure the DSD, called a DSG4
 126 disdrometer (Figure 1c), which meets the Functional Specification Requirements for
 127 Disdrometer issued by the China Meteorological Administration. This disdrometer has
 128 an HSC-OTT Parsivel2 sensor as the observation part, manufactured by OTT
 129 Messtechnik (Germany) and Huatron (China). When raindrops pass through the

130 horizontal flat laser beam generated by the transmitting part of the instrument, it causes
 131 signal attenuation in the laser observation area. The raindrop size is determined by the
 132 degree of signal attenuation and the falling speed is recorded by the transit time. The
 133 sampling time is 60s and the velocity and drop sizes are divided into 32 non-equally
 134 spaced bins, varying from 0.05 to 20.8 m s⁻¹ for velocity and 0.062 to 24.5 mm for drop
 135 diameter.

136 2.2 Quality control of the data

137 It was necessary to quality control the data because of potential instrument error.
 138 Every minute of DSD data collected by the six DSG4 disdrometers from May to
 139 October 2020 was carefully processed. Specifically, the following criteria were
 140 employed in choosing data for analysis(Jaffrain et al., 2011; Guyot et al., 2019; Pu et
 141 al., 2020): (1) the first two size bins were ignored because of low signal-to-noise ratio;
 142 (2) samples with 1-min total of raindrop number less than 10, or a rain rate at the
 143 moment of discontinuous observation less than 0.1 mmh⁻¹ were regarded as noise
 144 (corresponds to the second sample in Table 2); (3) raindrops with diameters more than
 145 8 mm were eliminated; (4) raindrops with a falling terminal velocity $V(D_i)$ that deviated
 146 from the empirical terminal velocity $V_{emp}(D_i)$ by more than 40% were removed (Kruger
 147 and Krajewski, 2002); and (5) samples with less than five bins after the correction of
 148 falling terminal velocity were deleted because their DSDs could not be determined with
 149 too few bins. The fourth criterion can be expressed by the formula:

$$150 \quad |V(D_i) - V_{emp}(D_i)| < 0.4V_{emp}(D_i) \quad (1)$$

151 where $V_{emp}(D_i) = 9.65 - 10.3\exp(-0.6D_i)$ (D_i is the mean volume-equivalent
 152 diameter of the i th size category), as derived from the formula given in Atlas et al.
 153 (1973).

154 After data quality control, the sample statistics of key steps are shown in Table 2.
 155 The number of 1-min DSD spectra selected from the six sites (LB, HS, TL, SD, BLG,
 156 DLD) after data quality control covering the rainy season (May–October) in the Qilian
 157 Mountains region in 2020 were 11103, 17619, 14814, 10736, 18861 and 13230,
 158 respectively, which accounted for 87.9%, 85.8%, 84.5%, 91.2%, 80.6% and 86.5% of
 159 the total number of samples.

160 Table 2. Sample statistics of data quality control at six sites

Samples	LB	HS	TL	SD	BLG	DLD
Total minutes (min)	12625	20536	17526	11770	23401	15289
Total minutes without noise (min)	12602	20509	17494	11756	23371	15267
After quality control (min)	11103	17619	14814	10736	18861	13230
Available data (%)	87.9%	85.8%	84.5%	91.2%	80.6%	86.5%

161

162 2.3 Integral parameters of rainfall

163 The basic observations obtained by the disdrometer were the counts of raindrops
 164 at each diameter and velocity. Also, the diameters given by the disdrometers were the
 165 mid value of two adjacent bins, which we take as the corresponding endpoint bin values.

166 The velocities were the weighted average velocity class over the corresponding
 167 disdrometer. The raindrop number concentration $N(D_i)$ ($\text{m}^{-3} \text{mm}^{-1}$) in the i th size bin
 168 per unit volume per unit size interval for diameter was calculated by the following
 169 equation:

$$170 \quad N(D_i) = \sum_{i,j=1}^{32} \frac{n_{i,j}}{A \cdot \Delta t \cdot V_j \cdot \Delta D_i} \quad (2)$$

171 where $n_{i,j}$ denotes the counts of raindrops measured by the disdrometer within size bin
 172 i and velocity bin j during the sampling time Δt ; A and Δt are the sampling area (0.0054
 173 m^2) and sampling time (60 s), respectively; V_j (m s^{-1}) is the mid-value falling speed for
 174 velocity bin j ; and ΔD_i is the diameter spread for the i th diameter bin.

175 Some integral rainfall parameters, such as the total number concentration N_t (m^{-3}),
 176 rain rate R (mm h^{-1}), radar reflectivity factor Z ($\text{mm}^6 \text{m}^{-3}$) and liquid water content W
 177 (g cm^{-3}), can be derived by the following equations:

$$178 \quad N_t = \sum_{i=1}^{32} N(D_i) \Delta D \quad (3)$$

$$179 \quad R = \frac{6\pi}{10^4 \rho_w} \sum_{i=1}^{32} V(D_i) D_i^3 N(D_i) \Delta D_j \quad (4)$$

$$180 \quad Z = \sum_{i=1}^{32} N(D_i) D_i^6 \Delta D_i \quad (5)$$

$$181 \quad W = \frac{\pi \rho_w}{6 \times 10^3} \sum_{i=1}^{32} D_i^3 N(D_i) \Delta D_i \quad (6)$$

182 where ρ_w is the water density (1.0gcm^{-3}); and $V(D_i)$ is the falling speed from the
 183 disdrometer. In this study, when calculating the rain rate we use $V_{emp}(D_i)$ to replace $V(D_i)$
 184 because of measurement error, particularly at larger bins and faster falling speeds,
 185 which is inspired from Tokay et al. (2014) and Zhang et al. (2019).

186 The characteristics of DSD can be described by a three-parameter gamma
 187 distribution in the form introduced by Ulbrich (1983). Also, it has better fitting
 188 capability than the M-P distribution on the broader variation of DSD fluctuations,
 189 including the middle rain drops, especially on small and large rain scales. The three-
 190 parameter gamma distribution can be expressed by the following formula:

$$191 \quad N(D) = N_0 D^\mu \exp(-\Lambda D) \quad (7)$$

192 where $N(D)$ is the raindrop number concentration; D is the raindrop bins with unit mm ;
 193 and N_0 , μ and Λ are the intercept, shape and slope parameter from the three parameters
 194 of the gamma model, which can be derived from gamma moments or the least-squares
 195 method, respectively. When $\mu=0$, it degenerates into the M-P DSD model.

196 Although, the gamma distribution is commonly accepted, the normalized gamma
 197 distribution has also been widely adopted with its independent parameters and clear
 198 physical meaning as follows (Dolan et al., 2018; Ma et al., 2019):

$$199 \quad N(D) = \frac{3}{128} N_w \left[\frac{(4 + \mu)^{(4+\mu)}}{\Gamma(4 + \mu)} \right] \left(\frac{D}{D_m} \right)^\mu \exp \left(\frac{-(4 + \mu)D}{D_m} \right) \quad (8)$$

200 where μ is the shape parameter, which is in dimensionless; D_m (mm) is the mass-
 201 weighted mean diameter, and N_w ($\text{m}^{-3} \text{mm}^{-1}$) is the normalized intercept parameter
 202 computed from D_m . The form is as follows:

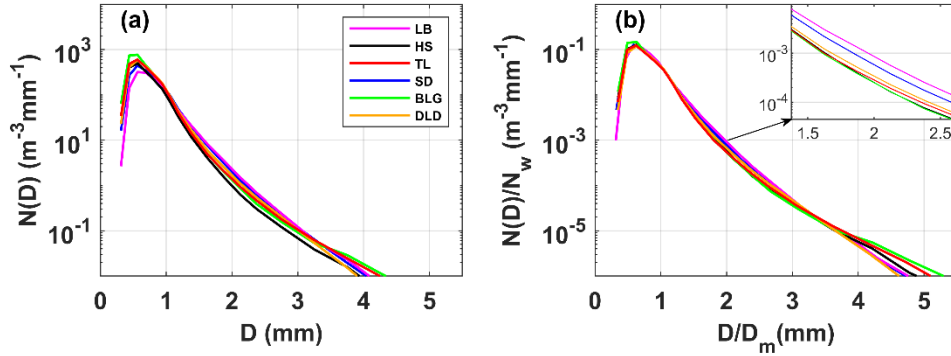
$$203 \quad D_m = \frac{\sum_{i=1}^{32} N(D_i) D_i^4 \Delta D_i}{\sum_{i=1}^{32} N(D_i) D_i^3 \Delta D_i} \quad (9)$$

$$204 \quad N_w = \frac{4^4}{\pi \rho_w} \left(\frac{10^3 W}{D_m^4} \right) \quad (10)$$

205 3 DSD parameter characteristics

206 3.1 Characteristics of DSD

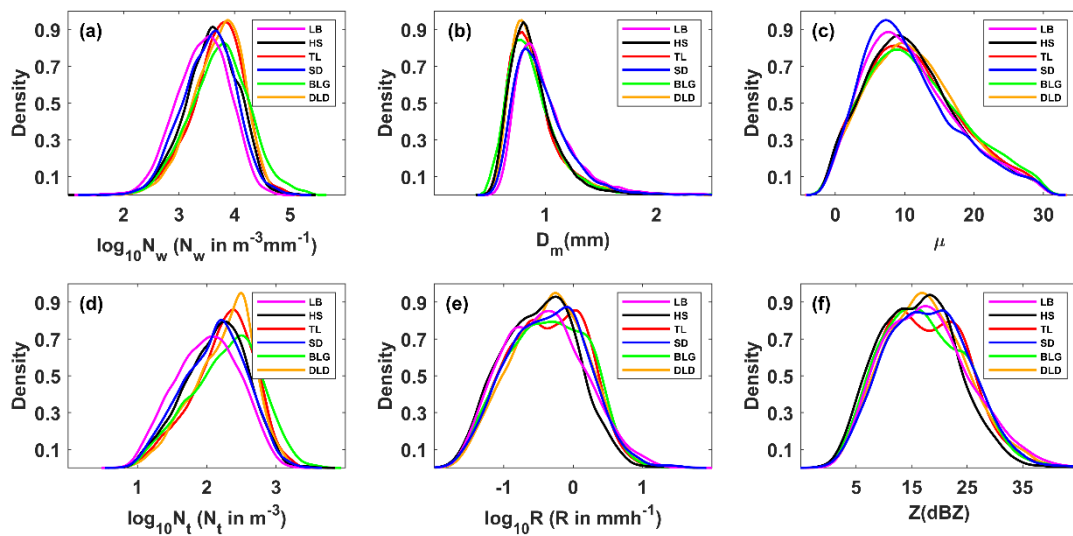
207 Figure 2a shows the mean DSDs for the six sites during the rainy season in the
 208 Qilian Mountains. The maximum concentration of raindrops was around 0.562 mm in
 209 diameter and the maximum number concentration values of sites were order as follows:
 210 BLG>TL>DLD>HS>SD>LB. As the diameter increased, the number concentration
 211 decreased and the concentration values followed the order
 212 LB>SD>DLD>TL>BLG>HS at around 2 mm in diameter. When the diameter was
 213 larger than 4 mm, the concentration at TL, BLG and HS was relatively high. In this
 214 study, the data were roughly divided into small raindrops (less than 1 mm in diameter),
 215 midsize raindrops (1–3 mm) and large raindrops (greater than 3 mm) to easily describe
 216 the difference in DSDs (Ma et al., 2019b; Pu et al., 2020). To highlight the DSD
 217 differences caused by the background environment, Figure 2b shows the mean DSDs
 218 normalized by the N_w and D_m results for the sites. Compared with Figure 2a, the
 219 raindrop characteristics were more consistent across sizes, while the differences
 220 between the sites were more pronounced, especially in the midsize and large raindrops,
 221 which truly reflected the DSD differences caused by the location. Combining the
 222 characteristics of the geographical environment of the six sites, we can analyze some
 223 differences in DSD characteristics in the Qilian Mountains. For small raindrops, the
 224 number concentrations at interior and southern-slope sites were greater than at northern-
 225 slope sites; for midsize raindrops, the number concentrations decreased sequentially at
 226 the northern-slope, southern-slope and interior sites; and for large raindrops, the number
 227 concentrations at the interior sites were larger. In addition, the number concentrations
 228 of raindrops in the middle section of this the mountainous area were slightly greater
 229 than those in the eastern section.



230
231 Figure 2. The (a) mean and (b) normalized mean DSDs at six sites in the Qilian
232 Mountains region in the rainy season

233 3.2 Distribution of DSD parameters

234 In order to study the differences in DSDs, we selected six integral rainfall
235 parameters for discussion—namely, the normalized intercept parameter (N_w), mass-
236 weighted mean diameter (D_m), shape parameter (μ), total number concentration (N_t),
237 rain rate (R) and radar reflectivity factor (Z). Figure 3 and Table 3 show the distributions
238 and statistics of these six DSD parameters (the distribution of each was normalized
239 using the uniform method). On average, D_m was more concentrated on smaller values
240 at HS and BLG, which showed smaller mean values than TL and DLD but significantly
241 more values greater than 1 mm at LB and SD; $\log_{10}N_w$ was more centralized on larger
242 values at TL and DLD, with relatively smaller values at LB and SD; and the distribution
243 patterns for μ and $\log_{10}N_t$ were similar to those for $\log_{10}N_w$. The density curves of R and
244 Z were similar, but there were differences among the six sites, which are analyzed in
245 detail later in the paper. It is noteworthy that the frequency of samples with R around
246 0.6–1.0 mm h⁻¹ was highest, and samples with R less than 1 mm h⁻¹ accounted for more
247 than half of the total rainfall.
248



249
250 Figure 3. Probability density distribution of integral DSD parameters at six sites (LB,
251 HS, TL, SD, BLG, DLD): (a) normalized intercept parameter $\log_{10}N_w$ (N_w in $m^{-3}mm^{-1}$);
252 (b) mass-weighted mean diameter D_m (mm); (c) shape parameter μ ; (d) total number

253 concentration $\log_{10}N_t$ (N_t in m^{-3}); (e) rain rate $\log_{10}R$ (R in mm h^{-1}); (f) radar reflectivity
 254 factor Z (dBZ)

255 Table 3. Statistical of several integral DSD parameters for all observations at six sites
 256 (LB, HS, TL, SD, BLG, DLD).

Sites	$\log_{10}N_w$			D_m			μ			$\log_{10}N_t$			R			Z		
	ME	SD	SK	ME	SD	SK	ME	SD	SK	ME	SD	SK	ME	SD	SK	ME	SD	SK
LB	3.43	0.47	-0.25	0.99	0.29	2.68	10.92	6.63	0.61	2.01	0.46	-0.07	0.94	1.90	0.23	17.79	7.82	0.44
HS	3.59	0.48	-0.29	0.89	0.25	3.35	11.12	6.64	0.53	2.13	0.45	-0.22	0.69	1.60	0.05	16.24	7.08	0.34
TL	3.69	0.48	-0.55	0.90	0.29	4.49	11.37	6.84	0.48	2.23	0.44	-0.43	0.89	1.48	-0.05	17.47	7.55	0.35
SD	3.54	0.48	-0.17	0.96	0.26	2.12	10.62	6.61	0.71	2.11	0.46	-0.17	0.97	2.01	0.06	17.95	7.47	0.28
BLG	3.72	0.54	-0.15	0.89	0.29	5.17	11.71	7.06	0.46	2.26	0.50	-0.25	0.94	2.13	-0.04	17.34	7.66	0.41
DLD	3.69	0.45	-0.50	0.90	0.25	2.66	11.52	6.66	0.43	2.24	0.43	-0.46	0.95	1.62	-0.01	17.70	7.43	0.37

257 Note: ME is mean; SD is standard deviation; SK is skewness.

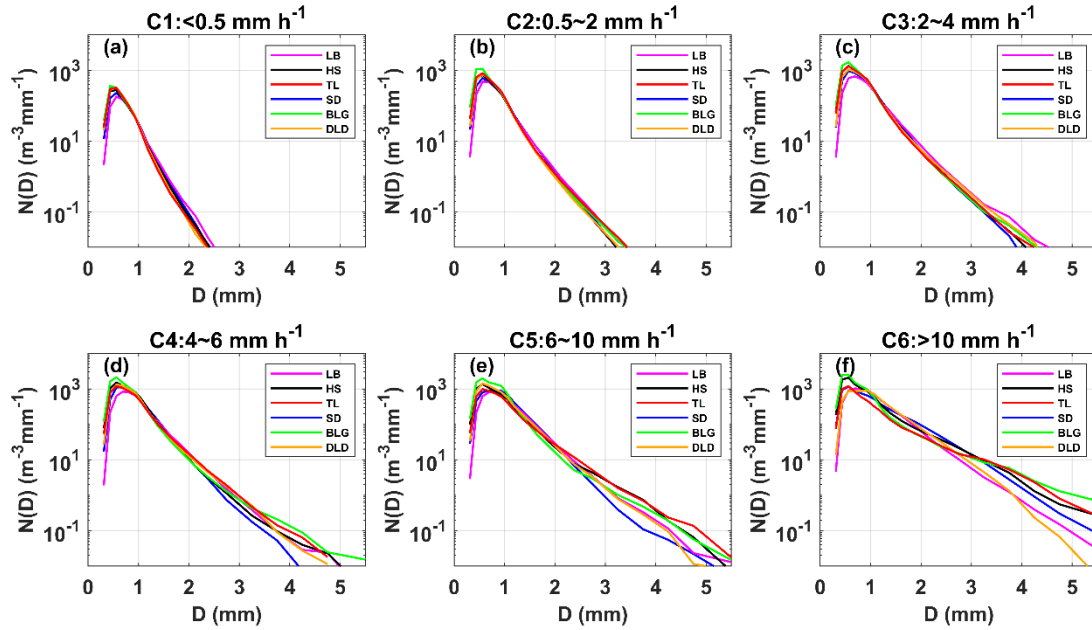
258 3.3 DSD characteristics in different rain rate classes

259 To further understand the characteristics of DSDs at the six sites, the samples were
 260 divided into six classes according to the associated rain rates (R): C1, $R < 0.5$; C2,
 261 $0.5 \leq R < 2$; C3, $2 \leq R < 4$; C4, $4 \leq R < 6$; C5, $6 \leq R < 10$; C6, $R \geq 10 \text{ mm h}^{-1}$. This classification
 262 was based on two considerations: firstly, the number of observation samples in different
 263 rainfall rates roughly conformed to a normal distribution; and secondly, the mean
 264 maximum diameter interval of different rainfall rates gradually increased (Li et al.,
 265 2019). Of course, other classification studies were referenced and the fact that the rain
 266 rate in this area is smaller than that in southern China was taken into account (Ma et al.,
 267 2019b; Zeng et al., 2021). Figure 4 shows the mean DSDs at each rainfall rate class for
 268 the six sites. Table 4 lists the number of samples and statistical values of the DSD
 269 parameters for the six classes. Clearly, as the rainfall rate increased, the number
 270 concentration of almost all raindrop sizes and the width of DSD shapes increased, and
 271 thus the tail of the DSD shape moved gradually towards a larger diameter, similar to
 272 previous findings, such as those of Ma et al. (2019b) and Pu et al. (2020). Taking a
 273 number concentration of $0.01 \text{ m}^{-3} \text{mm}^{-1}$, the mean maximum diameter of DSD in each
 274 class was ordered as follows: 2.3–2.5, 3.2–3.4, 3.9–4.5, 4.3–5.0, 5.0–5.6 and 6.0–7.0
 275 mm (the sixth-class diameter range is not fully shown in the figure). In class C1, the
 276 number concentrations were relatively similar at different sites; starting from class C2,
 277 the differences in number concentration increased when the diameter was greater than
 278 2 mm for the six sites; and the differences of in number concentration were gradually
 279 reflected in each raindrop size bin as the rainfall rate class increased. Observationally,
 280 the DSDs of BLG, HS and TL had larger number concentrations in different rainfall
 281 rate classes, and the DSD parameters and standard deviations (SDs) were larger,
 282 especially for BLG.

283 Table 4. Statistics of several integral DSD parameters for six rain rate classes at six sites.

Class	Sites	Samples	$\log_{10}N_w$	D_m	μ	$\log_{10}N_t$	R	Z
-------	-------	---------	----------------	-------	-------	----------------	-----	-----

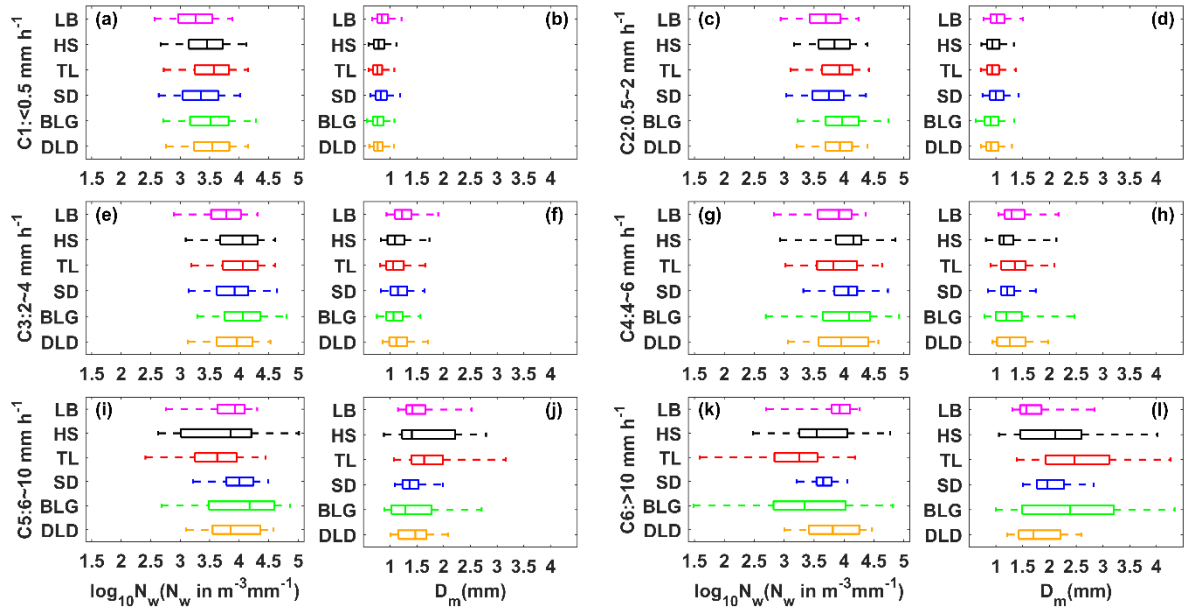
			ME	SD	ME	SD	ME	SD	ME	SD	ME	SD	ME	SD
C1(<0.5 mm h ⁻¹)	LB	6520	3.25	0.41	0.88	0.18	12.36	7.09	1.74	0.34	0.20	0.13	12.68	4.52
	HS	10753	3.43	0.44	0.81	0.17	12.01	7.03	1.89	0.37	0.20	0.13	11.90	4.54
	TL	7858	3.52	0.44	0.79	0.16	12.91	7.12	1.96	0.37	0.20	0.13	11.78	4.16
	SD	5772	3.34	0.43	0.85	0.18	11.72	6.99	1.82	0.36	0.20	0.13	12.51	4.40
	BLG	10073	3.50	0.48	0.79	0.17	12.94	7.28	1.94	0.40	0.20	0.13	11.73	4.26
	DLD	6891	3.51	0.43	0.79	0.15	13.04	6.92	1.96	0.36	0.21	0.13	12.14	4.15
C2(0.5~2 mm h ⁻¹)	LB	3318	3.66	0.41	1.06	0.24	9.93	5.75	2.30	0.28	1.00	0.41	22.55	3.27
	HS	5700	3.82	0.39	0.97	0.21	10.21	5.88	2.44	0.26	0.96	0.37	21.67	3.09
	TL	5368	3.87	0.42	0.98	0.23	10.35	6.15	2.49	0.26	1.07	0.41	22.18	3.33
	SD	3778	3.73	0.41	1.03	0.23	9.94	6.14	2.36	0.28	1.02	0.40	22.40	3.15
	BLG	6411	3.97	0.47	0.94	0.25	11.24	6.72	2.56	0.30	1.07	0.43	21.69	3.69
	DLD	4778	3.88	0.37	0.95	0.20	10.91	6.02	2.47	0.24	1.01	0.40	21.60	3.19
C3(2~4 mm h ⁻¹)	LB	782	3.71	0.47	1.31	0.37	7.33	4.28	2.52	0.29	2.77	0.56	29.54	2.87
	HS	884	3.96	0.50	1.16	0.34	8.42	5.22	2.73	0.27	2.76	0.54	28.33	3.06
	TL	1232	4.00	0.47	1.13	0.33	8.70	5.93	2.75	0.23	2.68	0.53	28.07	3.16
	SD	812	3.89	0.44	1.19	0.27	8.57	5.53	2.63	0.26	2.71	0.53	28.41	2.68
	BLG	1865	4.05	0.49	1.11	0.30	8.62	5.75	2.81	0.25	2.70	0.53	27.99	3.29
	DLD	1111	3.91	0.44	1.18	0.29	7.81	5.45	2.70	0.23	2.74	0.54	28.73	3.09
C4(4~6 mm h ⁻¹)	LB	229	3.80	0.47	1.41	0.40	7.33	3.94	2.65	0.31	4.76	0.57	32.69	2.63
	HS	191	4.03	0.54	1.28	0.47	7.54	4.42	2.86	0.27	4.80	0.56	31.70	3.34
	TL	213	3.84	0.56	1.41	0.51	6.23	4.64	2.77	0.28	4.77	0.54	32.82	3.54
	SD	187	4.03	0.41	1.24	0.27	8.35	5.02	2.80	0.22	4.76	0.54	31.32	2.52
	BLG	321	3.99	0.66	1.33	0.53	7.97	6.10	2.93	0.27	4.78	0.54	32.44	4.40
	DLD	270	3.92	0.53	1.35	0.47	6.50	4.80	2.83	0.25	4.83	0.56	32.55	3.47
C5(6~10 mm h ⁻¹)	LB	167	3.81	0.46	1.55	0.44	6.46	3.38	2.72	0.27	7.66	1.22	35.74	2.85
	HS	49	3.69	0.74	1.70	0.68	6.89	4.82	2.75	0.38	7.42	1.09	36.14	4.29
	TL	103	3.57	0.62	1.78	0.66	5.20	4.62	2.71	0.32	7.32	1.02	37.03	3.76
	SD	128	3.96	0.39	1.42	0.35	7.10	3.96	2.82	0.21	7.68	1.17	34.76	2.42
	BLG	138	3.97	0.76	1.51	0.80	8.34	6.35	2.99	0.27	7.37	1.02	35.09	4.96
	DLD	122	3.90	0.46	1.46	0.34	6.13	4.20	2.86	0.26	7.29	1.11	35.32	2.88
C6(>10 mm h ⁻¹)	LB	87	3.85	0.44	1.73	0.53	5.08	3.05	2.87	0.32	14.81	7.57	39.58	3.57
	HS	42	3.60	0.65	2.19	0.92	6.74	5.27	3.00	0.28	21.69	9.91	42.93	6.11
	TL	40	3.16	0.69	2.69	1.19	4.34	5.20	2.74	0.32	18.25	9.69	44.70	5.41
	SD	59	3.66	0.29	2.04	0.46	3.30	2.48	2.91	0.16	21.07	8.34	42.85	4.10
	BLG	53	3.38	0.93	2.58	1.52	5.58	6.19	3.00	0.37	21.95	9.05	44.08	7.50
	DLD	58	3.82	0.47	1.80	0.46	6.64	4.12	2.84	0.28	16.58	7.21	40.13	3.53



284

285 Figure 4. Distribution of mean measured DSD for different rain rate classes at six sites.

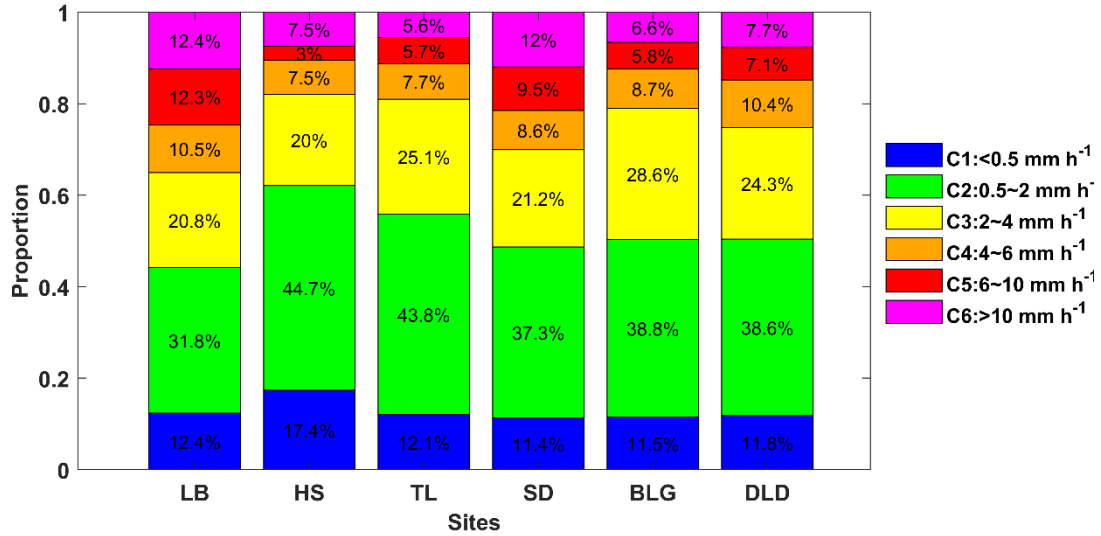
286 Figure 5 shows box-and-whisker plots of the normalized intercept parameter
 287 $\log_{10}N_w$ and mass-weighted mean diameter D_m for six sites in each rain rate class. The
 288 middle line in the box indicates the median. The left and right lines indicate the 25th and
 289 75th percentiles. The left and right ends of whiskers indicate the most extreme data
 290 points between the 5th and 95th percentiles, except outliers. The median D_m gradually
 291 increased with a larger value range as the rain rate class increased, particularly for HS
 292 and BLG in class C5 and C6. The median $\log_{10}N_w$ increased in class C1 to C3 and then
 293 tended to decrease in class C5 to C6, for which the reduction was obvious at sites with
 294 a larger value range, such as HS and BLG. Ma et al. (2019b) also obtained similar
 295 conclusions that D_m values increase with the increased rainfall intensity, while the
 296 $\log_{10}N_w$ is not as clear. The indication was that the increase in rain rate was mainly due
 297 to the growth in raindrop size. Also, the change in number concentration may have been
 298 caused by the imbalance between the loss of number concentration at small raindrop
 299 size and the addition at large raindrop sizes, which in a sense implies a relationship
 300 between the collision–coalescence and break–up of raindrops. It is worth noting that
 301 the microphysical processes were quite different among the sites, being greatly
 302 influenced by the surrounding environment. Because HS and BLG were located in the
 303 interior of the mountains and close to the ridge, their dynamics and thermodynamics as
 304 well underlying surfaces were thus different from those of other sites.
 305



306

307 Figure 5. Variation of the normalized intercept parameter $\log_{10}N_w$ (a) and the mass-
 308 weighted mean diameter D_m (b) for different rain rate classes at six sites. The three lines
 309 in the boxes are the 25th, 50th and 75th percentiles, from left to right, respectively. The
 310 whiskers at the left and right ends are the 5th and 95th percentiles, respectively. The
 311 colors represent the six sites as in other figures.

312 Figure 6 displays the contribution of different rain rate classes to the total rainfall
 313 at different sites. It is clear that C2 contributed the most to the total rainfall of all sites,
 314 followed by C3, and the sum of the two classes' contribution could reach 60% of the
 315 total rainfall. Compared with the interior and southern-slope sites, C2 and C3
 316 contributed slightly less to sites LB and SD (i.e., the northern slopes), while C5 and C6
 317 contributed relatively more to sites LB and SD, indicating that there is a greater
 318 probability of heavy precipitation events on the northern slopes. The DSD parameters
 319 in Table 3 provide a more detailed representation of the rainfall differences between the
 320 three geographical sections of the Qilian Mountains, i.e., the interior, southern slopes
 321 and northern slopes. Meanwhile, it also reflects the characteristics of rainfall in the
 322 eastern and interior sections, such as the eastern section had larger Z and D_m and smaller
 323 $\log_{10}N_w$ and $\log_{10}N_t$ compared to the interior. It is possible that there is a certain spatial
 324 connection between precipitation at the sites, related to factors such as the source of
 325 precipitation vapor, weather system and so on.



326

327 Figure 6. Proportion of rainfall with different rain rate classes to rain amount at six sites.

328 3.4 DSD properties for different rain types

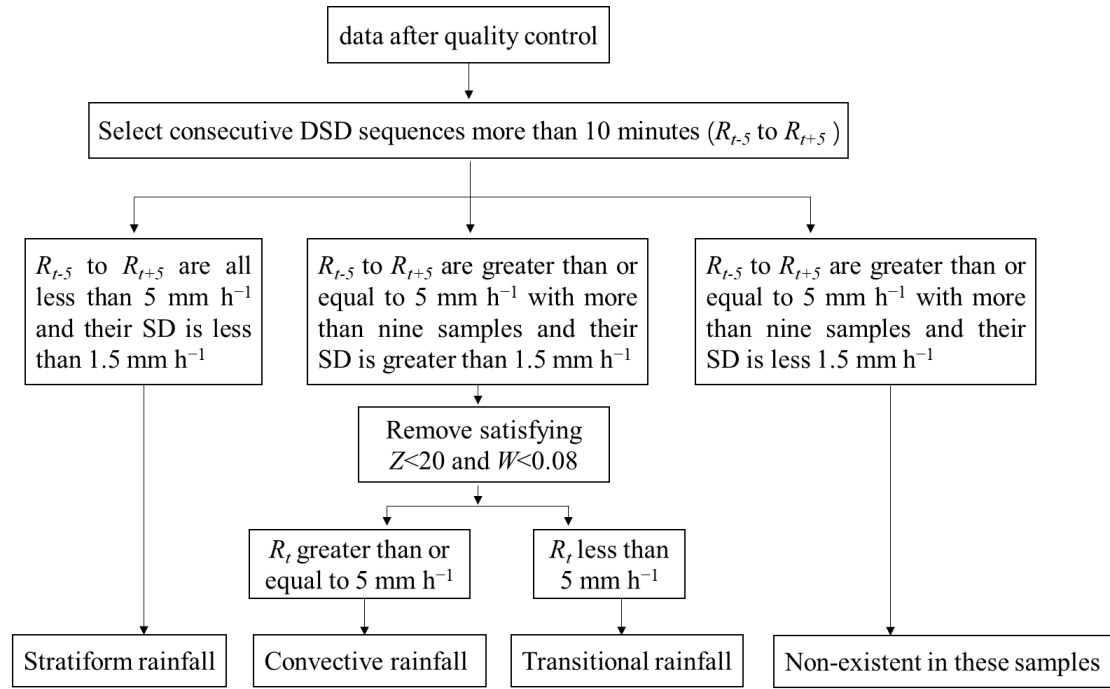
329

330 Previous studies on DSD have shown that there are significant differences in the
 331 DSD of convective and stratiform rainfall in the same climatic region, which has a
 332 substantial impact on the parameterization of NWP and remote sensing observations
 333 (Bringi et al., 2003; Penide et al., 2013). Due to the different physical mechanisms of
 334 convective and stratiform rainfall, it is possible to discuss the differences in
 335 microphysical structures for rainfall types through their DSD. Studies have employed
 336 many different classification methods for rainfall types; example, Testud et al. (2001)
 337 used the rain rate; Chen et al. (2013) combined the rain rate and its SD; and the findings
 338 of Das et al. (2018) were based on the rain rate and radar reflectivity factor. Among
 339 these, the method of Chen et al. (2013) has commonly been used to establish samples
 340 of convective and stratiform rainfall, but mainly in semi-humid or humid regions with
 341 relatively high rain rate and rainfall. However, the Qilian Mountains are located in the
 342 semi-arid regions of China and far from the sea, where the average rainfall rain and
 343 rainfall are quite different from in semi-humid regions. Therefore, this paper proposes
 344 a new classification method for precipitation applicable to the arid and semi-arid
 345 regions of Northwest China based on the classification ideas of Chen et al. (2013) and
 Das et al. (2018).

346

347 Firstly, the sequences of DSD with continuous 1-min samples more than 10 min
 348 are determined, and R_t is defined as the rain rate at time t . In the first case, the R
 349 of samples from R_{t-5} to R_{t+5} are all less than 5 mm h^{-1} and their SD is less than 1.5 mm
 350 h^{-1} ; in the second case, the R of samples from R_{t-5} to R_{t+5} are greater than or equal to 5
 351 mm h^{-1} with more than nine samples and their SD is greater than 1.5 mm h^{-1} ; and in
 352 the third case, the situation is the same as the second case but their SD is less 1.5 mm
 353 h^{-1} . Secondly, samples satisfying $Z < 20$ and $W < 0.08$ in the second case are removed
 354 (Thurai et al., 2016; Das et al., 2018). And then, samples with R_t greater than or equal
 355 to 5 mm h^{-1} in the second case are regarded as convective rainfall and samples with R_t
 less than 5 mm h^{-1} in the second case are regarded as transitional rainfall (the rainfall

356 stage in which convective precipitation develops and declines). Samples in the first case
 357 are regarded as stratiform rainfall. Through experiments, the third case does not exist.
 358 The main calculation process is shown in Figure 7



359

360

Figure 7. Classification method for rainfall types in the Qilian Mountains.

361

362

363

364

365

366

367

368

369

370

371

372

373

374

375

376

377

378

379

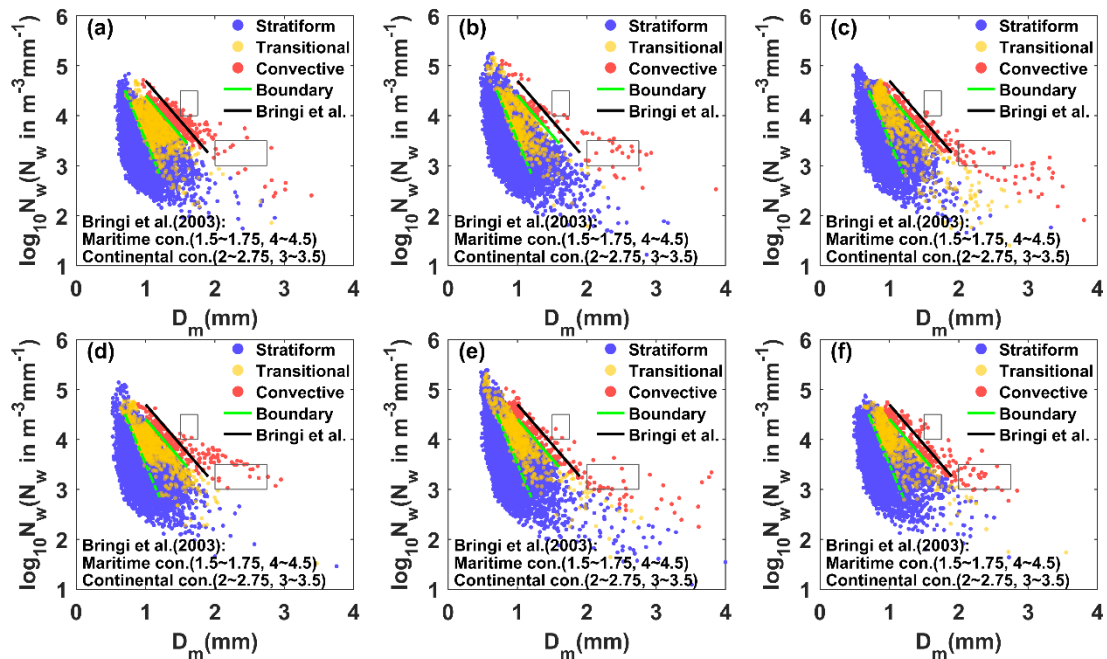
380

381

382

The $\log_{10}N_w$ and D_m of different rainfall types were different, which were taken as the main research objects. Figure 8 shows the variation of $\log_{10}N_w$ with D_m at different sites. The blue, red and yellow scatter points represent stratiform, convective and transitional rainfall, respectively. Obviously, there are fairly clear boundaries between the scatter points for the different precipitation type events, and the same dividing line can be used to distinguish between the different rainfall types at different sites. The green solid lines were drawn based on visual examination of the data with a slope of approximately -1.60 and intercept of 6.008 to represent the split between stratiform, transitional and convective rainfall in all subplots. The green dashed line can distinguish transitional rainfall (transitional and stratiform rainfall have an overlap area) with a slope of approximately -3.338 and intercept of 6.847 . Note that the dividing line between stratiform and convective rainfall has the same slope as that obtained by Brangi et al. (2003) (solid green line with a slope of -1.6 and intercept of 6.3), who fitted composite results based on disdrometer data and from radar retrievals covering many climate conditions from near the equator to plateau. The $\log_{10}N_w$ and D_m from the figures for stratiform, convective and transitional rainfall are respectively concentrated in the ranges of $3.1-3.9$, $0.75-1.1$ mm; $3.8-4.2$, $1.4-1.6$ mm; $3.6-4.0$, $1.05-1.2$ mm. Compared to the maritime-like cluster and continental-like cluster of convective rainfall proposed by Brangi et al. (2003), the convective events in the Qilian Mountains are not belong to continental-like cluster or maritime-like cluster, while the averages of D_m are slightly less than the continental-like cluster and the averages of $\log_{10}N_w$ are greater than the continental-like cluster. There are isolated convective events in the maritime-

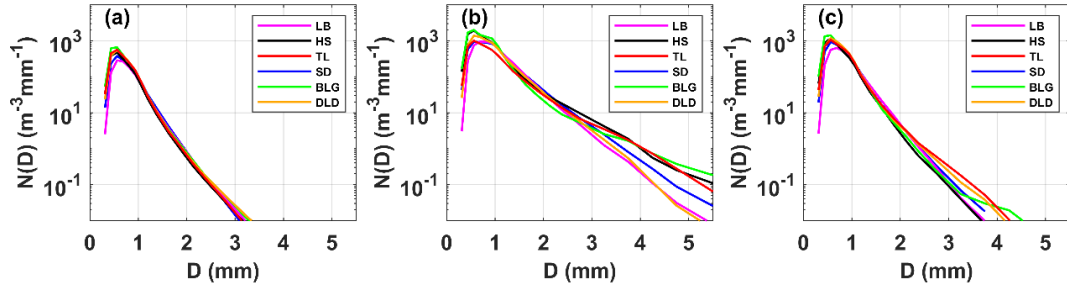
383 like cluster, but it is difficult to consistent with the features of the geographical location
 384 of the Qilian Mountains.
 385



386
 387 Figure 8. Scatter plot of $\log_{10}N_w$ versus D_m for different rain types at (a) LB, (b) HS, (c)
 388 TL, (d)SD, (e)BLG, and (f)DLD. The stratiform cases, convective cases and transitional
 389 cases are represented by blue, red and yellow scatter points, respectively. The green
 390 dashed lines are the $\log_{10}N_w$ - D_m relationship for stratiform versus convective cases and
 391 stratiform versus transitional case. The black dashed lines are the $\log_{10}N_w$ - D_m
 392 relationship for stratiform versus convective cases and stratiform versus transitional
 393 case from Bringi et al. (2003). The green dotted lines are the area of overlap between
 394 stratiform and transitional case.

395 Figure 9 shows the mean DSDs for stratiform, convective and transitional rainfall
 396 at the six sites. The range of number concentrations and corresponding raindrop
 397 diameters for the three types were significantly different, matching the basic
 398 characteristics of DSD. The mean DSDs of stratiform rainfall differed slightly among
 399 the sites; convective rainfall had big differences at among the sites; and transitional
 400 rainfall presented more differences beginning at larger than 2.2 mm in diameter, which
 401 were the expected results. Stratiform rainfall usually has a large horizontal extent and
 402 an homogeneous cloud distribution, which makes the DSD characteristics basically the
 403 same under the influence of the same cloud system in mountainous areas. However,
 404 convective rainfall is related to local thermal and dynamical factors, which could lead
 405 to differences in DSD at different sites when considering the complex topography and
 406 diverse underlying surfaces in mountainous areas. For example, for convective rainfall,
 407 there was a significant increase in the number concentration of raindrops larger than 2.2
 408 mm in diameter at BLG, HS and TL, indicating that these sites are conducive to the
 409 development of convective precipitation. Also, the number concentration of small
 410 raindrops at BLG and HS were higher than at TL (the southern slope), which may be

411 due to the higher altitude of the interior sites reducing the falling distance of raindrops
 412 after exiting the cloud and decreasing the impact of collision on the raindrop evolution.
 413 In other words, even for the same rainfall type, the microphysics of rainfall at different
 414 sites is still different, depending on the topography and position of the observation point
 415 relative to the cloud base.



416
 417 Figure 9. Distribution of mean measured DSD for (a) stratiform rainfall, (b) convective
 418 rainfall and (c) transitional rainfall at six sites.

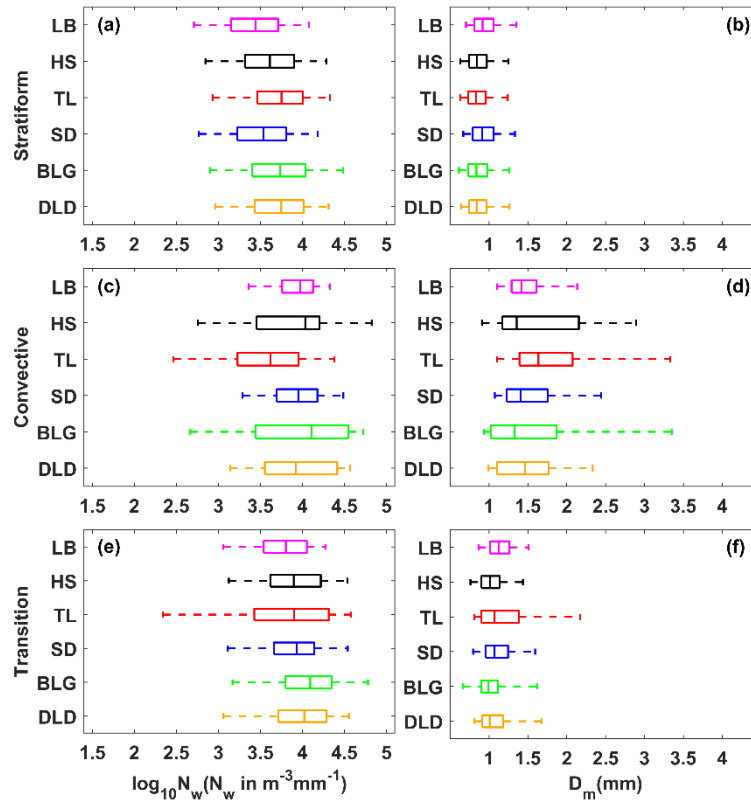
419 Figure 10 shows box-and-whisker plots of $\log_{10}N_w$ and D_m for different rain types.
 420 The $\log_{10}N_w$ and D_m of stratiform rainfall were smaller than those of convective rainfall
 421 but larger than those of transitional rainfall. Sites with a large $\log_{10}N_w$ value range had
 422 larger value ranges for D_m ; and sites with a large median $\log_{10}N_w$ had a smaller median
 423 D_m , especially at sites HS and BLG for convective rainfall. Based on the mean values
 424 of the six sites in Table 5, the DSD characteristics in the Qilian Mountains consist of a
 425 larger N_w and smaller D_m (compared the results of studies in other regions, seeing
 426 discussion section for details) due to the melting of tiny, compact graupel, and rimed
 427 ice particles (relative to large, low-density snowflakes). Compared with transitional
 428 rainfall, the D_m of convective rainfall was obviously larger, indicating that the increase
 429 in rain rate in this area is mainly due to the growth in raindrop size. Moreover, on the
 430 northern slopes one should consider the increase in number concentration, because the
 431 $\log_{10}N_w$ of convective rainfall also increased. Note that the number of convective
 432 samples on the northern slopes was higher than that of other sites, which corresponds
 433 to the speculation regarding the contribution of different rain rate classes. On average,
 434 for stratiform rainfall, the dispersion degree of $\log_{10}N_w$ and D_m at different sites was
 435 8.3% and 10.0%, respectively; and for convective rainfall it was 10.4% and 23.4%. The
 436 SDs of DSD parameters at sites HS and BLG were relatively large.

437 Table 5 Statistics of several integral DSD parameters for six sites with stratiform rainfall,
 438 convective rainfall and transitional rainfall

Type	Sites	No. samples	$\log_{10}N_w$		D_m		μ		$\log_{10}N_t$		R		Z	
			ME	SD	ME	SD	ME	SD	ME	SD	ME	SD	ME	SD
S	LB	7123	3.42	0.42	0.96	0.21	11.48	7.98	1.98	0.38	0.54	0.60	16.93	5.93
	HS	12694	3.60	0.44	0.88	0.21	11.24	7.89	2.14	0.40	0.54	0.58	16.17	6.06
	TL	10091	3.71	0.43	0.87	0.20	11.90	8.01	2.23	0.39	0.65	0.67	16.85	6.15
	SD	7175	3.51	0.44	0.95	0.22	11.15	8.03	2.07	0.39	0.62	0.64	17.36	6.10

	BLG	12467	3.72	0.49	0.88	0.23	12.24	8.50	2.25	0.44	0.70	0.74	17.11	6.33
	DLD	9685	3.70	0.42	0.88	0.21	11.91	7.91	2.23	0.38	0.67	0.69	17.18	6.13
C	LB	292	3.91	0.35	1.49	0.35	6.50	3.30	2.81	0.23	9.28	5.56	35.88	3.59
	HS	100	3.85	0.67	1.71	0.84	6.33	4.33	2.95	0.30	12.55	13.75	37.32	6.64
	TL	159	3.54	0.59	1.87	0.74	5.21	4.97	2.72	0.30	9.48	6.91	37.96	5.21
	SD	219	3.91	0.37	1.54	0.47	6.61	4.68	2.85	0.19	10.75	7.68	36.24	5.02
	BLG	198	3.91	0.74	1.64	0.97	8.00	7.37	3.00	0.27	10.57	15.49	36.29	6.75
	DLD	203	3.94	0.48	1.50	0.43	6.96	5.24	2.87	0.27	9.41	6.04	35.89	4.27
T	LB	787	3.76	0.39	1.15	0.21	8.37	4.35	2.47	0.31	2.16	1.25	26.42	3.89
	HS	541	3.89	0.49	1.05	0.29	8.98	6.74	2.59	0.33	1.81	1.15	24.79	3.89
	TL	465	3.77	0.70	1.22	0.49	8.81	6.91	2.56	0.44	2.30	1.21	27.10	4.39
	SD	819	3.87	0.41	1.12	0.26	8.23	5.46	2.59	0.28	2.28	1.18	26.59	4.04
	BLG	665	4.04	0.51	1.04	0.31	10.33	7.31	2.72	0.33	2.19	1.13	25.66	4.44
	DLD	503	3.95	0.46	1.10	0.30	8.69	6.16	2.67	0.31	2.35	1.17	26.60	4.20

439



440

441

Figure 10. As in Fig. 5 but for different rain types at six sites.

442

3.5 Implications for radar rainfall estimation with DSD

443

444

445

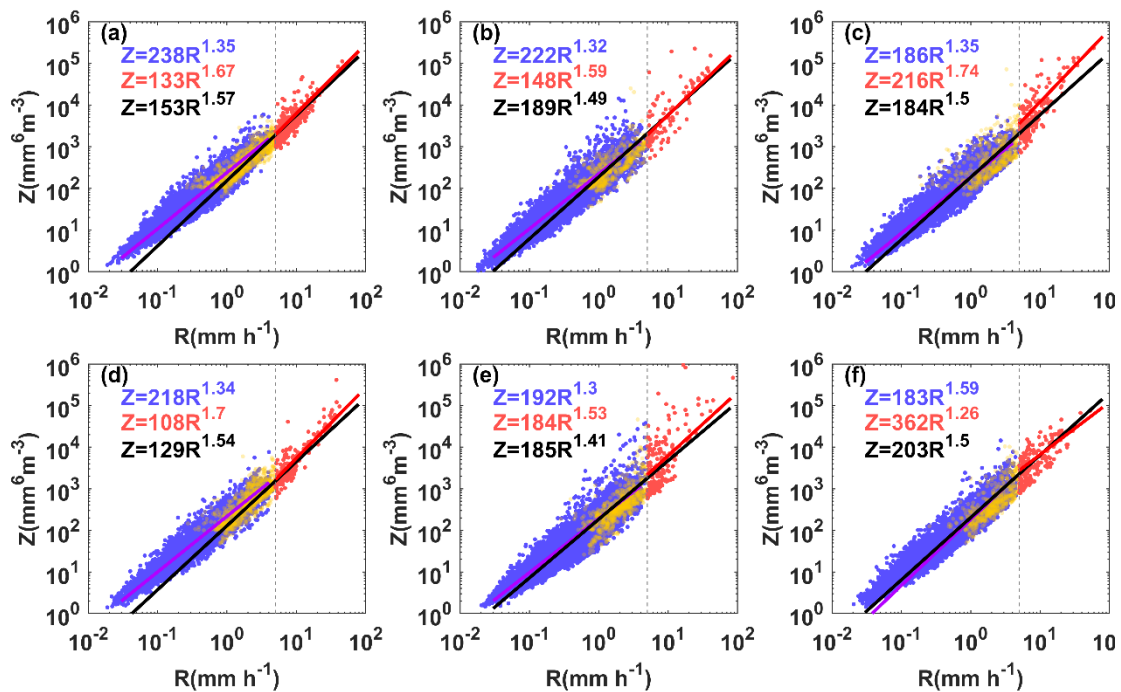
446

447

The sixth moment of raindrop diameter is proportional to the radar reflectivity factor and the 3.76th moment is approximately the rain rate (they can be calculated by Equations 4 and 5). Generally, the theoretical basis of QPE for single polarization radar (ground-based or space-based) is the power relationship between the radar reflectivity and rainfall rate ($Z=AR^b$). This makes the coefficients A and exponents b of the power

448 relationship heavily dependent on the variation in DSD. Therefore, it is necessary to
 449 obtain the A and b of different sites according to different rainfall types.

450 Figure 11 shows the Z - R scatter plots for different sites and the fitted power-law
 451 relationships for different rainfall types. The blue and red scatter points represent
 452 stratiform and convective rainfall, respectively. The purple, red and black solid lines
 453 indicate the Z - R relationships for stratiform, convective and total rainfall, respectively.
 454 It shows that the Z - R scatter points for HS and BLG were relatively scattered around
 455 the 5 mm h^{-1} rain rate. Besides, the Z - R relationship of total rainfall underestimated the
 456 stratiform rainfall at low R values and the convective rainfall at high R values. Based
 457 on the average Z - R relationship using a least-squares method, the dispersion degree of
 458 A and b at different sites was 42.5% and 10.7%, respectively, which reveals there to be
 459 large differences in mountain areas.
 460

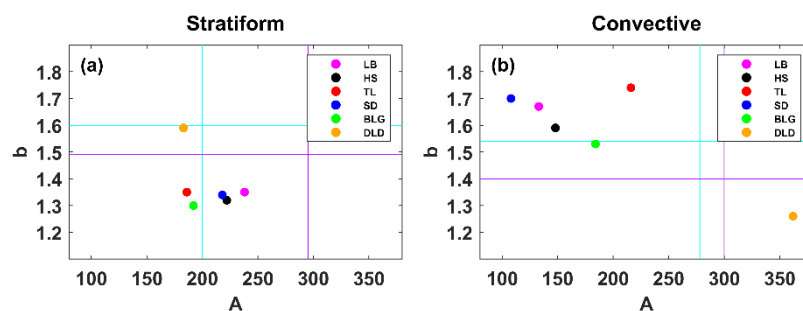


461

462 Figure 11. Scatter plots of Z ($\text{mm}^6 \text{m}^{-3}$) versus R (mm h^{-1}) for three rain types at (a) LB,
 463 (b) HS, (c) TL, (d)SD, (e)BLG, and (f)DLD. The blue, red and yellow scatter points,
 464 represent stratiform, convective and transitional cases, respectively. The purple, red and
 465 black lines denote the Z - R relations. The blue, red and black formula denote stratiform,
 466 convective and total Z - R relationships. The grey dashed line indicates r is 5 mmh^{-1}

467 In order to compare the six sites Z - R relationships with some standard Z - R
 468 relationships, the results for $Z=300R^{1.4}$ for convective rainfall commonly used in radar,
 469 and $Z=200R^{1.6}$ (i.e., M48) for stratiform rainfall commonly used in midlatitude areas,
 470 are provided in Figure 12. Overall, convective rainfall had smaller values of A and
 471 larger values of b than those of stratiform rainfall (excluding DLD). The A values of
 472 convective rainfall were smaller than the commonly used Z - R relationship with large
 473 differences, but the b values were greater. The distribution of A and b for stratiform
 474 rainfall was relatively concentrated, with A and b ranging from 186–238 and 1.3–1.35,

475 respectively. The A values of stratiform rainfall were close to those of M48, and the b
 476 values were close to and smaller than the Z - R of global stratiform rainfall. Site DLD
 477 had a similar Z - R for stratiform rainfall with as M48, while its convective rainfall was
 478 different from other sites, with a larger A value (twice as large as other sites) and smaller
 479 b value, which probably relates to its own local climatic influences formed in a narrow
 480 valley with higher peaks on either side relative to TL site that would cause more
 481 precipitation~~which probably relates to its own local climatic influences formed in a~~
 482 ~~narrow valley~~. In addition, it is clear that the A value of stratiform rainfall increased
 483 from the southern slopes to northern slopes, while the opposite was the case for
 484 convective rainfall. Also, the Z - R relationships of the same section are more consistent,
 485 such as those of the interior or the northern slopes, which have distinct geographic
 486 characteristics.



487
 488 Figure 12. The A and b values of the Z - R relationships for (a) stratiform rainfall and (b)
 489 convective rainfall at six sites. The purple lines in (a) and cyan lines in (b) correspond
 490 to the global Z - R model ($Z = 295R^{1.49}$ for continental stratiform rainfall and $Z = 278R^{1.54}$
 491 for convective rainfall, respectively) (Ghada et al., 2018). The cyan lines in (a) represent
 492 the midlatitude stratiform rainfall Z - R model ($Z = 200R^{1.60}$, Marshall, 1948); and the
 493 purple lines in (b) represent the convective rainfall Z - R model ($Z = 300R^{1.40}$) applied to
 494 operational weather radar (Fulton et al., 1998).

495 4 Discussion

496 The paper analyses the statistical characteristics of DSD at different sites in the
 497 Qilian Mountains during the rainy season, which not only contain rainfall classes using
 498 the ideal velocity value in the calculation formula of R and rainfall types but more
 499 importantly reflect the differences between different sites. The results from different
 500 aspects can be mutually confirmed and have a good representation of the spatial
 501 distribution, serving as a strong factual basis for discussion of the microphysical
 502 structure of precipitation. For example, with the rain rate class rising, the number
 503 concentration of all size bins is increased and the width of DSDs became wider, which
 504 manifested as convective rainfall having a larger rain rate. In spatial terms, the
 505 characteristics of precipitation in the interior of the mountains and on the southern
 506 slopes were closer, whether considering the overall DSD distribution or the
 507 distributions of DSD parameters. However, there were obvious variabilities at the
 508 interior sites for DSD parameters due to the influences of local dynamics and thermal
 509 effects. On the other hand, these characteristics also exhibited some differences between
 510 the interior and eastern sections of the Qilian Mountains, especially in the discussion of

511 DSD parameters for rainfall classes and rainfall types (s Figures 5 and 10). This spatial
512 variation in DSD suggests that microphysical processes involved in the DSD are
513 influenced by complex topography (altitude, mountain alignment) and potentially
514 related to the source of water vapor, development of precipitation process and
515 anthropogenic factors.

516 Compared to previous studies that focused on eastern [3.48 for $\log_{10}N_w$ and 1.23
517 mm for D_m , Pu et al.(2020)], southern [3.86 for $\log_{10}N_w$ and 1.47 mm for D_m , Zhang et
518 al.(2019)], northern [3.60 for $\log_{10}N_w$ and 1.15 mm for D_m , Ma et al.(2019b)] and central
519 [3.48 for $\log_{10}N_w$ and 1.54 mm for D_m , Fu et al.(2020)] China as well the Tibetan
520 Plateau[3.47 for $\log_{10}N_w$ and 1.05 mm for D_m , Wang et al.(2021)], the Qilian Mountains
521 region has its own unique DSD characteristics and Z-R relationship during the rainy
522 season, including a smaller raindrop diameter with a higher number concentration [3.69
523 for $\log_{10}N_w$ and 0.94 mm for D_m]. Moreover, the division of rainfall rate classes in the
524 Qilian Mountains more adequately reflects the DSD characteristics in each class, unlike
525 when using the classification method of other sites with larger rainfall rates. More
526 importantly, the proposed classification of stratiform and convective rainfall can clearly
527 distinguish between the distribution of $\log_{10}N_w$ versus D_m in different rainfall types, for
528 which the dividing line (slope of -1.6 and intercept of 6.008) between stratiform and
529 convective rainfall has the same slope as the line (slope of -1.6 and intercept of 6.3)
530 given by Bringi et al (2003). Furthermore, according to this method, it can be proven
531 that convective events are not belong to the continental-like cluster or maritime-like
532 cluster, conforming to the unique precipitation characteristics of the Qilian Mountains .

533 As mentioned above, the characteristics of DSD mainly describe diameters larger
534 than 0.2 mm, which is limited by the observation instruments being unable to detect
535 small drops of diameter less than 0.2 mm. Therefor, it is not a complete DSD, and the
536 number concentration of small drops of diameter less than 0.5 mm is underestimated.
537 Recent studies have been devoted to improving DSD observations in order to overcome
538 the limitations of disdrometers. A study by Thurai et al. (2017) obtained a more
539 complete DSD by splicing 2DVD and MPS (Meteorological Particle Spectrometer)
540 measurements to observe DSDs and developed a technology to reconstruct the drizzle-
541 mode DSD (Raupach et al., 2019), which a good presentation of the DSD of small
542 raindrops was provided, and important applications were highlighted.

543 **5 Summary and conclusion**

544 Based on six months of DSD data observed over the southern slopes, northern
545 slopes and interior of the Qilian Mountains, the characteristics and differences of DSD
546 were studied, and the Z-R relationships of six sites were discussed. The main
547 conclusions can be summarized as follows:

548

- 549 1. For all rainfall events, the number concentrations of small and large raindrops in
550 the interior and on the southern slopes were greater than that on the northern slopes,
551 while midsize raindrops were less. The DSD of the interior of the mountains
552 showed great variability, mainly in terms of the $\log_{10}N_w$ and D_m (DSD parameters),
553 which was quite different to the case for the northern slopes.

- 554 2. The rainfall rates were divided into six categories based on the DSD characteristics:
555 C1, $R < 0.5$; C2, $0.5 \leq R < 2$; C3, $2 \leq R < 4$; C4, $4 \leq R < 6$; C5, $6 \leq R < 10$; and C6, > 10
556 mm h^{-1} . As the rainfall rate increased, the differences in number concentration of
557 each raindrop size became significantly larger, especially at the interior sites.
558 Besides, classes C5 and C6 made a relatively large contribution to the northern
559 slopes, with a greater probability of heavy precipitation events.
- 560 3. The dispersion degree of $\log_{10}N_w$ and D_m at the six sites was 8.3% and 10.0% for
561 stratiform rainfall and 10.4% and 23.4% for convective rainfall, respectively. It is
562 easier to increase the number concentration of large raindrops in the interior area
563 of the mountains during convective rainfall. Meanwhile, there is a greater increase
564 in the number concentration of raindrops over the northern slopes during
565 convective rainfall.
- 566 4. The dispersion degree of coefficient A and exponent b in the Z - R relationship for
567 the six sites was 42.5% and 10.7%, respectively. Overall, the Z - R relationships of
568 the ipsilateral sites were more consistent; and the A value of stratiform rainfall
569 increased from the southern slopes to northern slopes, while the opposite was true
570 for convective rainfall. The Z - R relationships in stratiform rainfall were similar
571 and generally underestimated by the $Z=200R^{1.6}$ model used for midlatitude
572 stratiform rainfall; and the Z - R relationships for convective precipitation varied
573 greatly at different sites, which were overestimated by $Z=300R^{1.4}$ at lower rain
574 rates values and underestimated at higher rain rates values.

575 This study reveals the microphysical variability of precipitation over the complex
576 topography of the arid and semi-arid regions of Northwest China, which can not only
577 improve local numerical simulations, but also provides a basis for further understanding
578 the differences in DSD characteristics formed at the mesoscale due to topographic
579 factors and the water vapor distribution, etc. This study holds importance as a basis for
580 the future implementation of weather modification techniques, which is of great
581 significance in solving the shortage of water resources in the arid and semi-arid regions.

582 *Data availability.* Disdrometer data used in this study are available by contacting the
583 authors.

584 *Author contributions.* WM conducted the detailed analysis; WZ provided financial
585 support and conceived the idea; MK collated the observation data; all the authors
586 contributed to the writing and revisions.

587 *Competing interests.* The authors declare that they have no conflict of interest.

588 **Acknowledgments**

589 The work was supported by Weather modification ability construction project of
590 Northwest China under grant No. ZQC-R18208 and The Second Tibetan Plateau

591 Comprehensive Scientific Expedition Grant No. 2019QZKK0104. Thanks are given to
592 Asi Zhang for her help in discussing some questions. The authors also thank reviewers
593 and editors for their helpful suggestion for this study

594 **References**

- 595 Adirosi, E., N. Roberto, M. Montopoli, E. Gorgucci, and L. Baldini, 2018: Influence of
596 disdrometer type on weather radar algorithms from measured DSD: Application
597 to Italian climatology. *Atmosphere*, 9, 360.
- 598 Angulo-Martínez, M., and A. Barros, 2015: Measurement uncertainty in rainfall kinetic
599 energy and intensity relationships for soil erosion studies: An evaluation using
600 PARSIVEL disdrometers in the Southern Appalachian Mountains.
601 *Geomorphology*, 228, 28-40.
- 602 Atlas, D., R. Srivastava, and R. S. Sekhon, 1973: Doppler radar characteristics of
603 precipitation at vertical incidence. *Reviews of Geophysics*, 11, 1-35.
- 604 Bringi, V., V. Chandrasekar, J. Hubbert, E. Gorgucci, W. Randeu, and M. Schoenhuber,
605 2003: Raindrop size distribution in different climatic regimes from disdrometer
606 and dual-polarized radar analysis. *Journal of the atmospheric sciences*, 60, 354-
607 365.
- 608 Campos, E., I. Zawadzki, M. Petitdidier, and W. Fernandez, 2006: Measurement of
609 raindrop size distributions in tropical rain at Costa Rica. *Journal of Hydrology*,
610 328, 98-109.
- 611 Chen, B., J. Yang, and J. Pu, 2013: Statistical characteristics of raindrop size
612 distribution in the Meiyu season observed in eastern China. *Journal of the*
613 *Meteorological Society of Japan. Ser. II*, 91, 215-227.
- 614 Dolan, B., B. Fuchs, S. Rutledge, E. Barnes, and E. Thompson, 2018: Primary modes
615 of global drop size distributions. *Journal of the Atmospheric Sciences*, 75, 1453-
616 1476.
- 617 Das, S., and A. Maitra, 2018: Characterization of tropical precipitation using drop size
618 distribution and rain rate-radar reflectivity relation. *Theoretical and applied*
619 *climatology*, 132, 275-286.
- 620 Fu, Z., and Coauthors, 2020: Statistical characteristics of raindrop size distributions and
621 parameters in Central China during the Meiyu seasons. *Journal of Geophysical*
622 *Research: Atmospheres*, 125, e2019JD031954.
- 623 Fulton, R. A., J. P. Breidenbach, D.-J. Seo, D. A. Miller, and T. O'Bannon, 1998: The
624 WSR-88D rainfall algorithm. *Weather and forecasting*, 13, 377-395.
- 625 Geoffroy, O., A. Siebesma, and F. Burnet, 2014: Characteristics of the raindrop
626 distributions in RICO shallow cumulus. *Atmospheric Chemistry and Physics*, 14,
627 10897-10909.
- 628 Ghada, W., A. Buras, M. Lüpke, C. Schunk, and A. Menzel, 2018: Rain microstructure
629 parameters vary with large-scale weather conditions in Lausanne, Switzerland.
630 *Remote Sensing*, 10, 811.
- 631 Giannetti, F., and Coauthors, 2017: Real-time rain rate evaluation via satellite downlink
632 signal attenuation measurement. *Sensors*, 17, 1864.
- 633 Gou, X., F. Chen, M. Yang, J. Li, J. Peng, and L. Jin, 2005: Climatic response of thick
634 leaf spruce (*Picea crassifolia*) tree-ring width at different elevations over Qilian
635 Mountains, northwestern China. *Journal of Arid Environments*, 61, 513-524.

636 Guyot, A., Pudashine, J., Protat, A., Uijlenhoet, R., Pauwels, V., Seed, A., and Walker,
637 J. P., 2019: Effect of disdrometer type on rain drop size distribution
638 characterisation: A new dataset for south-eastern Australia. *Hydrology and Earth*
639 *System Sciences*, 23, 4737-4761.

640 Han, H., Zhang, Y., Tian, J. et al. 2023: Raindrop Size Distribution Measurements at
641 High Altitudes in the Northeastern Tibetan Plateau during Summer. *Adv. Atmos.*
642 *Sci.* 40, 1244–1256.

643 Jash, D., E. Resmi, C. Unnikrishnan, R. Sumesh, T. Sreekanth, N. Sukumar, and K.
644 Ramachandran, 2019: Variation in rain drop size distribution and rain integral
645 parameters during southwest monsoon over a tropical station: An inter-comparison
646 of disdrometer and Micro Rain Radar. *Atmospheric Research*, 217, 24-36.

647 Jaffrain, J., and Berne, A., 2011: Experimental quantification of the sampling
648 uncertainty associated with measurements from PARSIVEL disdrometers. *Journal*
649 *of Hydrometeorology*, 12, 352-370.

650 Kruger, A., and W. F. Krajewski, 2002: Two-dimensional video disdrometer: A
651 description. *Journal of Atmospheric and Oceanic Technology*, 19, 602-617.

652 Le Loh, J., D.-I. Lee, and C.-H. You, 2019: Inter-comparison of DSDs between
653 Jincheon and Miryang at South Korea. *Atmospheric Research*, 227, 52-65.

654 Li, Z., and Coauthors, 2019: Climate background, relative rate, and runoff effect of
655 multiphase water transformation in Qilian Mountains, the third pole region.
656 *Science of The Total Environment*, 663, 315-328.

657 Lim, Y. S., J. K. Kim, J. W. Kim, B. I. Park, and M. S. Kim, 2015: Analysis of the
658 relationship between the kinetic energy and intensity of rainfall in Daejeon, Korea.
659 *Quaternary International*, 384, 107-117.

660 Ma, L., L. Zhao, D. Yang, Y. Xiao, L. Zhang, and Y. Qiao, 2019a: Analysis of Raindrop
661 Size Distribution Characteristics in Permafrost Regions of the Qinghai–Tibet
662 Plateau Based on New Quality Control Scheme. *Water*, 11, 2265.

663 Ma, Y., G. Ni, C. V. Chandra, F. Tian, and H. Chen, 2019b: Statistical characteristics of
664 raindrop size distribution during rainy seasons in the Beijing urban area and
665 implications for radar rainfall estimation. *Hydrology and Earth System Sciences*,
666 23, 4153-4170.

667 Marshall, J. S., 1948: The distribution of raindrops with size. *J. meteor.*, 5, 165-166.

668 McFarquhar, G. M., T.-L. Hsieh, M. Freer, J. Mascio, and B. F. Jewett, 2015: The
669 characterization of ice hydrometeor gamma size distributions as volumes in N_0 –
670 λ – μ phase space: Implications for microphysical process modeling. *Journal of*
671 *Atmospheric Sciences*, 72, 892-909.

672 Narayana Rao, T., N. Kirankumar, B. Radhakrishna, and D. Narayana Rao, 2006: On
673 the variability of the shape-slope parameter relations of the gamma raindrop size
674 distribution model. *Geophysical research letters*, 33.

675 Protat, A., and Coauthors, 2019: The latitudinal variability of oceanic rainfall properties
676 and its implication for satellite retrievals: 1. Drop size distribution properties.
677 *Journal of Geophysical Research: Atmospheres*, 124, 13291-13311.

678 Pu, K., X. Liu, Y. Wu, S. Hu, L. Liu, and T. Gao, 2020: A comparison study
679 of raindrop size distribution among five sites at the urban scale during the
680 East Asian rainy season. *Journal of Hydrology*, 590, 125500, <https://doi.org/10.1016/j.jhydrol.2020.125500>.
681

682 Penide, G., A. Protat, V. V. Kumar, and P. T. May, 2013: Comparison of two
683 convective/stratiform precipitation classification techniques: Radar reflectivity
684 texture versus drop size distribution–based approach. *Journal of Atmospheric and
685 Oceanic Technology*, 30, 2788-2797.

686 Qin, Y., H. Lei, D. Yang, B. Gao, Y. Wang, Z. Cong, and W. Fan, 2016: Long-term
687 change in the depth of seasonally frozen ground and its ecohydrological impacts
688 in the Qilian Mountains, northeastern Tibetan Plateau. *Journal of Hydrology*, 542,
689 204-221.

690 Rincon, R. F., and R. H. Lang, 2002: Microwave link dual-wavelength measurements
691 of path-average attenuation for the estimation of drop size distributions and rainfall.
692 *IEEE Transactions on geoscience and remote sensing*, 40, 760-770.

693 Raupach, T. H., M. Thurai, V. Bringi, and A. Berne, 2019: Reconstructing the drizzle
694 mode of the raindrop size distribution using double-moment normalization.
695 *Journal of Applied Meteorology and Climatology*, 58, 145-164.

696 Seela, B. K., J. Janapati, P. L. Lin, K. K. Reddy, R. Shirooka, and P. K. Wang, 2017: A
697 comparison study of summer season raindrop size distribution between Palau and
698 Taiwan, two islands in western Pacific. *Journal of Geophysical Research:
699 Atmospheres*, 122, 11,787-711,805.

700 Smith, J. A., E. Hui, M. Steiner, M. L. Baeck, W. F. Krajewski, and A. A. Ntelekos,
701 2009: Variability of rainfall rate and raindrop size distributions in heavy rain.
702 *Water Resources Research*, 45.

703 Thurai, M., P. Gatlin, and V. Bringi, 2016: Separating stratiform and convective rain
704 types based on the drop size distribution characteristics using 2D video
705 disdrometer data. *Atmospheric Research*, 169, 416-423.

706 Thurai, M., P. Gatlin, V. Bringi, W. Petersen, P. Kennedy, B. Notaroš, and L. Carey,
707 2017: Toward completing the raindrop size spectrum: Case studies involving 2D-
708 video disdrometer, droplet spectrometer, and polarimetric radar measurements.
709 *Journal of Applied Meteorology and Climatology*, 56, 877-896.

710 Testud, J., S. Oury, R. A. Black, P. Amayenc, and X. Dou, 2001: The concept of
711 “normalized” distribution to describe raindrop spectra: A tool for cloud physics
712 and cloud remote sensing. *Journal of Applied Meteorology*, 40, 1118-1140.

713 Tian, H., T. Yang, and Q. Liu, 2014: Climate change and glacier area shrinkage in the
714 Qilian mountains, China, from 1956 to 2010. *Annals of Glaciology*, 55, 187-197.

715 Tokay A, Wolff D B, Petersen W A, 2014. Evaluation of the New Version of the Laser-
716 Optical Disdrometer, OTT Parsivel². *Journal of atmospheric and oceanic
717 technology*, 31, 1276-1288.

718 Ulbrich C W., 1983: Natural variations in the analytical form of the raindrop size
719 distribution. *Journal of climate and applied meteorology*, 22, 1764-1775.

720 Wainwright, C. E., D. T. Dawson, M. Xue, and G. Zhang, 2014: Diagnosing the
721 intercept parameters of the exponential drop size distributions in a single-moment
722 microphysics scheme and impact on supercell storm simulations. *Journal of*
723 *Applied Meteorology and Climatology*, 53, 2072-2090.

724 Wang, Y., J. Zheng, Z. Cheng, and B. Wang, 2020: Characteristics of Raindrop Size
725 Distribution on the Eastern Slope of the Tibetan Plateau in Summer. *Atmosphere*,
726 11, 562.

727 Wu, Y., and L. Liu, 2017: Statistical characteristics of raindrop size distribution in the
728 Tibetan Plateau and southern China. *Advances in Atmospheric Sciences*, 34, 727-
729 736.

730 Yang, L., J. Smith, M. L. Baeck, B. Smith, F. Tian, and D. Niyogi, 2016: Structure and
731 evolution of flash flood producing storms in a small urban watershed. *Journal of*
732 *Geophysical Research: Atmospheres*, 121, 3139-3152.

733 Zhang, A., and Coauthors, 2019: Statistical characteristics of raindrop size distribution
734 in the monsoon season observed in southern China. *Remote Sensing*, 11, 432.

735 Zhao, P., and Coauthors, 2019: The Tibetan Plateau surface-atmosphere coupling
736 system and its weather and climate effects: The Third Tibetan Plateau Atmospheric
737 Science Experiment. *Journal of Meteorological Research*, 33, 375-399.

738 Zeng, Y., and Coauthors, 2021: Statistical Characteristics of Raindrop Size Distribution
739 during Rainy Seasons in Northwest China. *Advances in Meteorology*, 2021.

740